processes

MDPI

Article

Photocatalytic Degradation of Neonicotinoids—A Comparative Study of the Efficacy of Hybrid Photocatalysts

Rahmiye Zerrin Yarbay [1,2,*], Veli Şimşek [1,3], Lucija Bogdan [4] and Vesna Tomašić [4]

[1] Department of Chemical Engineering, Faculty of Engineering, Bilecik Şeyh Edebali University, 11230 Bilecik, Turkey; veli.simsek@bilecik.edu.tr
[2] Energy Technologies Application and Research Centre, Bilecik Şeyh Edebali University, 11210 Bilecik, Turkey
[3] Biotechnology Application and Research Centre, Bilecik Şeyh Edebali University, 11230 Bilecik, Turkey
[4] Faculty of Chemical Engineering and Technology, University of Zagreb, 10000 Zagreb, Croatia; lbogdan@fkit.hr (L.B.); vtomas@fkit.hr (V.T.)
* Correspondence: zerrin.yarbay@bilecik.edu.tr

Abstract: This study deals with the synthesis and characterization of a series of hybrid photocatalysts consisting of different loadings of TiO_2, Cd, and Fe on mesoporous SBA-15 material. The prepared samples were characterized by Fourier transform infrared spectroscopy (FT-IR), X-ray diffraction (XRD), and scanning electron microscopy (SEM), and tested for the removal of the neonicotinoid insecticide imidacloprid. The results showed that uncalcined 10% Cd-SBA-15 catalyst exhibited the best photocatalytic activity. The photocatalytic degradation of the imidacloprid was carried out in a batch photoreactor at different pH values, and in the presence or absence of additional compounds such as peroxymonosulfate (PMS) and peroxydisulfate (PDS). The best degradation results were achieved at a pH value of 6.5 with 10% Cd/SBA-15. The degradation performance increased with the addition of PMS and PDS. Based on the results of the experimental measurements, Cd/SBA-15 is a good candidate that can show a reasonable degradation efficiency and reactivity, especially in the presence of PDS or PMS.

Keywords: photocatalytic degradation; photocatalysts; imidacloprid; TiO_2/SBA-15; Cd/SBA-15; Fe/SBA-15

check for updates

Citation: Yarbay, R.Z.; Şimşek, V.; Bogdan, L.; Tomašić, V. Photocatalytic Degradation of Neonicotinoids—A Comparative Study of the Efficacy of Hybrid Photocatalysts. *Processes* **2024**, *12*, 489. https://doi.org/10.3390/pr12030489

Academic Editor: Maria Jose Martin de Vidales

Received: 16 January 2024
Revised: 22 February 2024
Accepted: 23 February 2024
Published: 28 February 2024

1. Introduction

Water pollution caused by long-term pesticide use is a global problem. In recent years, efforts have been made to test new technologies, synthesis methods, and oxidation processes to remove pesticide residues [1,2]. Neonicotinoid insecticides are a relatively new generation of chemical compounds developed for commercial purposes. Since their discovery, they have been widely used due to their systemic nature and selective activity on nicotinicacetylcholinereceptors (*nAChRs*) of insects [3]. Well-known representatives of neonicotinoids include imidacloprid (IMI), acetamiprid (ACE), and thiacloprid (TIA), among others [4]. Registered patterns of use of imidacloprid (IMI) in agriculture now include traditional foliar spray application, as well as soil drench application, drip irrigation, trunk (injection) application, stem or granular treatments, and seed treatments [5]. Because of its wide-scale use and persistence in the environment, the elimination of IMI residues has become a target of recent research.

In the last three decades, advanced oxidation processes (AOPs) have emerged as an important area of research to eliminate environmental pollution. These processes primarily rely on the generation of highly reactive hydroxyl radicals (•OH) and other reactive oxygen species (ROSs) in situ, which are formed in the reaction medium through different mechanisms depending on the basic design and method of process implementation. Recently, more attention has been paid to the optimization of heterogeneous photocatalysis, which is an AOP and uses solid photocatalysts to treat pollutants in the aqueous phase [6]. These processes have proven successful in the removal of various organic compounds, including pesticides [7]. It should be emphasized that the applicability of AOPs largely depends on the degree of wastewater contamination, in addition to the toxicity of the compound to be removed and the availability of a suitable method to generate •OH and other ROSs, such as superoxide ion radicals ($O_2^{\bullet-}$), and singletoxygen ($^1O_2$), which are very efficient for the degradation of various organic pollutants. Compared with conventional AOPs, which are mostly based on $^\bullet$OH as the main oxidizing agent, persulfate-based AOPs (PS-AOPs) rely on the activation of peroxymonosulfate (PMS, HSO_5^-) and/or peroxydisulfate (PDS, $S_2O_8^{2-}$) to generate highly reactive sulfate radicals ($SO_4^{\bullet-}$). The activation of PS can be achieved through various methods, including UV photoactivation, thermal activation or heating, microwave, electrochemical, and transition metal ions/metal oxide treatment [8]. Nevertheless, AOPs based on the application of semiconductor photocatalysis show great potential for practical application in the treatment of waste gases and wastewater, groundwater remediation, and water disinfection [9].

As common semiconductor materials and photocatalysts such as TiO_2, ZnO, CdS, and g-C_3N_4 cannot provide active sites for the efficient degradation of pollutants, several strategies are employed. The use of defect engineering methods and the replacement of surface functional groups on semiconductor materials play an extremely important role, as this can extend the optical absorption of existing materials [10–12].

Despite numerous investigations involving different types of photocatalysts and various research strategies, the limited visible light absorption and rapid recombination of photo generated charge carriers are still major problems in photocatalysis. For this reason, modern research is focused on the development of new functionalized materials to extend light harvesting, promote charge transfer, and increase the photocatalytic activity. Recently, new functional materials, such as $Ti_3C_2T_x$ (T_x = OH, O or F as terminal surface groups), i.e., TiO_2-based MXene materials, have been investigated with promising photocatalytic features ascribed to the generated oxygen vacancies (OVs), exceptional metallic conductivity of the $Ti_3C_2T_x$-MXene precursor, and tunable optical properties [13]. On the other hand, Wei et al. found that highly dispersed single cobalt-anchored onto the 2-methylimidazole modified carbon nitride (Co-MCAMeIm) exhibits an excellent photocatalytic performance in activated PMS for the degradation of sulfamethoxazole (SMX) as a target pollutant [14]. Wang et al. applied a novel activation strategy that relies on the use of crystalline carbon nitride (CCN) and visible light (Vis) to activate periodate (PI) for the highly efficient removal of ciprofloxacin. It was found that crystalline carbon nitride (CCN) has a stronger light absorption and more efficient charge carrier separation and mobility than polymerized carbon nitride (PCN), resulting in more efficient charge carrier separation and mobility than PCN [15]. Recently, research has focused on the preparation of advanced materials obtained by combining existing photocatalytic materials, especially those that are photoactive in the visible range, with zeolites, mesoporous materials, and metal-organic frameworks (MOFs); porous silica microspheres; and multi-component oxide microspheres, taking advantage of the complementary benefits of the different materials [10–12].

Mesoporous materials based on silicates have the amorphous properties of gels and an ordered crystal structure. These materials are becoming increasingly important in the removal of organic pollutants because they can be adapted to the desired molecules by specific changes in synthesis methods and can be economically regenerated and reused. Commonly used silicate-based mesoporous materials are those with small pores, hexagonally arranged MCM-41 (MCM, Mobil Composition of Matter) and cubically arranged MCM-48, and those with larger pores, hexagonal SBA-15 (SBA, Santa Barbara Amorphous) and cubic SBA-16, as well as other hexagonal mesoporous silicates [16]. From the comparison of MCM-41 and SBA-15 mesoporous materials, it can be seen that SBA-15 has a much broader distribution of pore sizes, i.e., unlike MCM-41 with a one-dimensional (1D) structure of mesoporous channels; SBA-15 has micropores and small mesopores at the intersections of channels and mesoporous [17]. Mesoporous silicates are good adsorbents due to their ordered structure with a uniform distribution of pore sizes (2–50 nm), allowing for the selective adsorption of small molecules [18,19]. The large specific surface area (up to 1600 m^2/g) and large pore volume are responsible for the high adsorption capacity of mesoporous silicate materials. The ion exchange of various metals such as Al, Ga, In, Zn, and Cd; transition metals such as Ti, V, Fe, Cu, Nb, Mo, and Zr; and rare metals such as La and Ce into the structure of MCM- 41 has attracted the attention of numerous researchers [20].

This study deals with SBA-15, which is very promising as a potential carrier for semiconductor nanoparticles due to its large specific surface area, high absorption capacity, and facilitation of reactivation [21]. Semiconductors can be incorporated into the mesoporous silicate structure in two ways: (a) directly during synthesis or (b) by a suitable post-synthesis method. The choice of the appropriate method results in different types of isolated or active sites on the surface of the mesoporous walls or inside the channels of the mesoporous structure. Sharma et al. [22] found that 10% TiO_2 on Al-MCM-41 and SBA-15 showed a higher degradation rate of the herbicide isoproturon compared with TiO_2, and attributed this to the absence of particle agglomeration and light scattering/dispersion on the TiO_2 surface. Sadjadi et al. [23] and Anandan [24] investigated TiO_2/MCM-41 as a photocatalyst for dye degradation (MO), and found that TiO_2 immobilized on a silicate surface was more effective than colloidal TiO_2 nanoparticles. In addition, the researchers claimed that the mesoporous structure delocalizes the electrons originating from the excitation of the semiconductor material and thus delays the recombination of electrons and holes, creating an effective environment for a greater number of surface active sites, ultimately leading to more efficient photodegradation. However, it was also found that the incorporation of TiO_2 into the silicate structure of MCM-41 and SBA-15 can lead to a disruption of the mesoporous network, especially at higher mass fractions of TiO_2. Furthermore, it was concluded that the formation of highly dispersed anatase TiO_2 particles on the outer surface was responsible for the enhancement of the photoactivity of composite photocatalysts.

Considering the unresolved problems found in previous research and the unique advantages of mesoporous materials, this work aims to prepare and test the activities of different composites based on mesoporous SBA-15 as potential photocatalysts for the photodegradation of a model neonicotinoid insecticide. The composite samples were prepared with the aim of prolonging light absorption, promoting charge transfer to increase irradiation absorption, and increasing the active surface area through the presence of mesoporous materials, resulting in the absorption of light of lower energy and longer wavelengths, i.e., photo activation under conditions of simulated solar radiation or in the range close to the visible part of the electromagnetic spectrum. Different hybrid photocatalysts based on mesoporous SBA-15 and additional compounds such as TiO_2, Cd, and Fe were tested in the imidacloprid removal system and compared with pure SBA-15. The synthesized catalysts were characterized by X-ray diffraction analysis (XRD), Fourier-transform infrared spectroscopy (FT-IR), and scanning electron microscopy with energy dispersive X-ray spectroscopy (SEM/EDX) together with mapping.

2. Materials and Methods

2.1. Chemicals and Reagents

All of the chemicals used in this work were of analytical reagent grade. Initial solutions of IMI were prepared by dissolving an appropriate amount of IMI (Sigma Aldrich Company Ltd., Osijek, Croatia) in ultra-pure water (18.2 $M\Omega\ cm^{-1}$) produced through a Nirosta Ultrapure Water System (Nirosta, Osijek, Croatia). To adjust the initial water−IMI solution pH, sulfuric acid (H_2SO_4) or sodium hydroxide (NaOH) supplied from VWR International S.A.S., Fontenay-sous-Bois, France, was used. HPLC-grade acetonitrile and formic acid (98%, p.a.) were purchased from VWR International, Radnor, PA, USA. For SBA-15 synthesis, Pluronic P123 (Poly(ethylene glycol)-block-poly(propylene glycol)-block-poly(ethylene glycol)) (144mL, 1.7M-Sigma Aldrich) and tetraethyl orthosilicate (TEOS, SKYGEN, Adana, Türkiye) were used.

2.2. Preparation of SBA-15 and Hybrid Photocatalysts

In this work, the TiO_2/SBA-15 hybrid catalyst was synthesized using the hydrothermal method [25]. On the other hand, SBA-15, Cd/SBA-15, and Fe/SBA-15 were synthesized through the in situ incorporation method using the procedures described in the literature [26–29]. To obtain pure SBA-15, a solution of the surfactant Pluronic P123 (Poly(ethylene glycol)-block-poly(propylene glycol)-block-poly(ethylene glycol))(144 mL, 1.7 M-Sigma Aldrich) in water was obtained and amounts of water and Pluronic P123 were adjusted as described earlier [29]. After stirring at 313K for 4 h, tetraethyl orthosilicate (TEOS, Merck) was added to the solution and the resulting solution was further stirred for 2h. The molar ratio of TEOS/Pluronic P123 was fixed at 2 h during the syntheses. Aging of the solution at 373 K for 48 h resulted in the formation of a crystalline solid. After a washing step with deionized water and a drying step at 353 K for 12 h, the synthesis of SBA-15 was completed by calcination at 813 K for 5 h. The synthesis of Cd-Fe/SBA-15 catalysts followed the procedure described above, modified by the simultaneous addition of active precursors ($CdSO_4$ and Fe_2O_3, respectively) and the silica source (TEOS). The amount of active material was determined based on the mass ratios of Cd, Fe, and Ti of cadmium sulfate powder ($CdSO_4$: Cd), iron III oxide (Fe_2O_3-Sigma Aldrich: Fe), and titanium dioxide (TiO_2: Ti) to Si of TEOS. Finally, the catalysts were calcined at 623 K for 5 h. The synthesis steps of SBA-15 and photocatalysts (Cd/SBA-15, Fe/SBA-15, and TiO_2/SBA-15) are shown in Figure 1. The Fe/Si and Cd/Si ratios were determined as 25%, 10%, and 25% in the synthesis of the metal/SBA-15 catalysts. Moreover, different TiO_2 loading ratios (58.33, 74.30, and 81.23%) were determined for the synthesis of TiO_2/SBA-15.

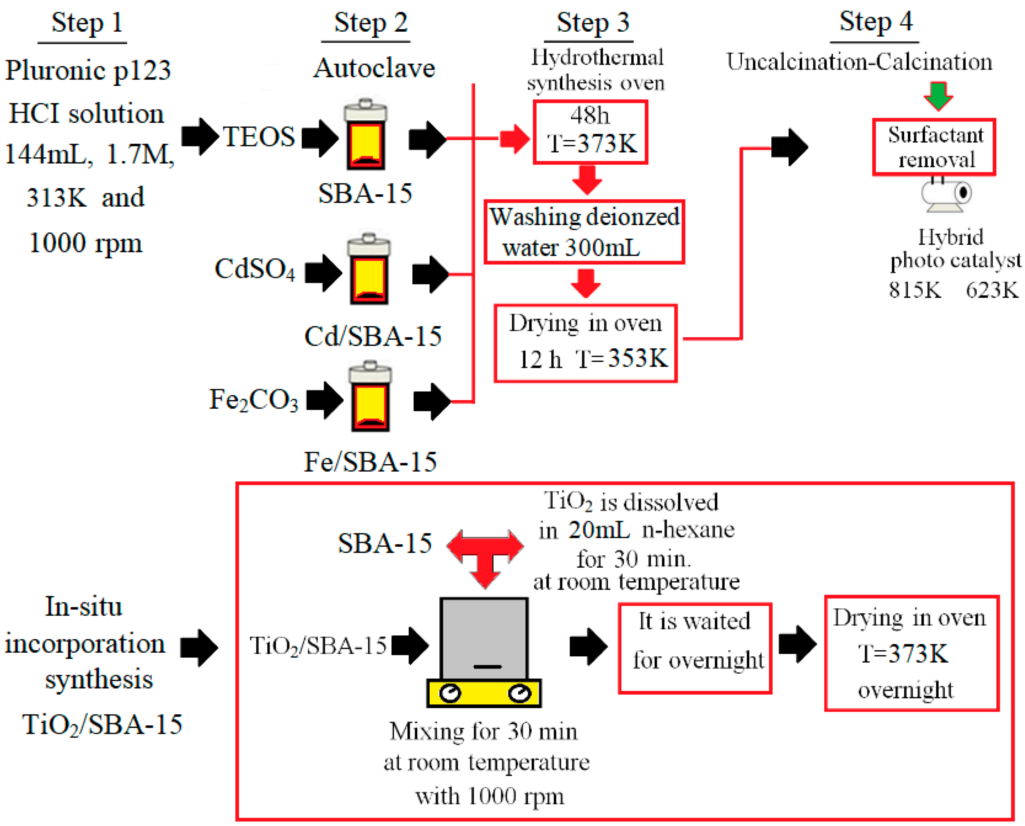

Figure 1. Schematic diagram of different stages in the preparation of the studied samples.

2.3. Characterization of the Prepared Samples

The physicochemical properties of the prepared samples were determined using various instrumental techniques such as FT-IR, XRD, SEM/EDX, and mapping. FT-IR analyses of the SBA-15, TiO_2/SBA-15, Cd/SBA-15, and Fe/SBA-15 samples were carried out using the Attenuated Total Reflectance (ATR) technique with the Perkin Elmer IR device between wavelengths of 380 and 4000 cm^{-1}. The Panalytical Empryan HT-XRD instrument was used to determine the phase structures of the synthesized hybrid photocatalyst. All of the samples of the hybrid photocatalysts were examined by XRD at 40 kV (current) and 30 V (tension) using CuKα (ʎ = 1.540) radiation with a step size of 0.066 and a range of $0° < 2\theta < 90°$. Moreover, to determine the elemental composition, elemental dispersion, and surface morphological structure of the hybrid photocatalysts, SEM/EDX, and mapping analyses were carried out using the Zeiss SUPRA V 40 instrument (BARUM, Bilecik, Türkiye).

2.4. Photolytic and Photocatalytic Experiments

The photocatalytic activities of the prepared composite photocatalysts were tested using a UVA Pen-Ray lamp (UVP-Ultra Violet products, Cambridge, UK; UVA 400–315 nm; Pen-Ray lamp model 90-0019-01 with λ_{max} = 365 nm) placed vertically in the central part of the reactor in a side quartz cuvette. The UVA irradiation intensity was measured periodically with the UVP radiometer and the corresponding sensor was about 3.78 mW cm^{-2}. Before the photocatalytic test, the adsorption equilibrium between the surface of the photocatalyst and the organic solution was determined (the solution was kept in the dark for 30 min). All of the photocatalytic measurements were performed in a suspension photo reactor at an initial IMI concentration of 10 ppm, with a total reactor volume of 80 mL and with 80 mg of photocatalyst. Initial solutions of IMI were prepared by dissolving an appropriate amount of IMI (Sigma Aldrich Company Ltd.) in ultrapure water (18.2 MΩ cm^{-1}) produced through a Nirosta Ultrapure Water System (Nirosta, Osijek, Croatia). The reaction solution was mixed with a magnetic stirrer at room temperature (298K) at a speed of 250 rpm. The adsorption measurements were carried out in the same reaction system under identical operating conditions, but without an irradiation source, while the photolytic experiments were carried out in the absence of photocatalysts. For every experiment, the pH value was measured at the beginning and end of each experiment using a pH meter. The initial pH of the solution was adjusted to 6.5 or 3.5. by adding 0.1 M sodium hydroxide (NaOH) or 0.1 M sulfuric acid (H_2SO_4) (supplied from VWR International S.A.S., Fontenay-sous-Bois, France). Prior to the photocatalytic measurements, the stability of the Cd-based hybrid photocatalyst, i.e., the possible leaching of Cd, was tested using a simple method based on deposition with Na_2S.

The changes in IMI concentration were monitored using a Shimadzu high-performance liquid chromatography (HPLC) equipped with a UV/Vis detector (SPD-20A) using an Agilent Zorbax SB-C18 column (250 × 4.6 mm, 5 µm). The working temperature of the column was set at 313K and changes in IMI concentrations were monitored at a wavelength of 260 nm. Gradient elution was carried out using 95%water and 5% acetonitrile with 0.3% formic acid as mobile phase A and 5% water and 95% acetonitrile with 0.3% formic acid as mobile phase B at a flow rate of 1 mL min^{-1}. Acetonitrile (HPLC grade) was purchased from VWR Chemicals and formic acid (98%, p.a.) from Lach-Ner. At specified time intervals, 1 mL aliquots of the reaction mixture were taken and filtered through a 0.22 µm PVDF syringe filter (FilterBio®, Labex Ltd., Budapest, Hungary) to avoid the presence of catalyst particles in the samples for HPLC analysis and damage to the column. To gain better insight into the mechanism of IMI degradation over the mesoporous hybrid photocatalyst, a procedure similar to that used for the photocatalytic test was performed, but with the addition of additional agents such as potassium persulfate (PDS; 5 mmol L^{-1}) and potassium monosulfate (PMS; 5 mmol L^{-1}) as the external electron acceptors and the sources of sulfate radicals ($\bullet SO_4^-$). To test the stability and reusability of the photocatalyst, some photocatalytic experiments were repeated several times. After each run, the photocatalyst sample was removed from the solution, washed with deionized water, and dried at room temperature for 4 h.

3. Results and Discussion

3.1. XRD Analysis

Figure 2 shows the results of the low and high-angle XRD analysis of the SBA-15 and the hybrid samples consisting of different loadings of TiO_2, Fe, and Cd on SBA-15. Similar results are shown in our previous work dealing with the activities of Cd/SBA-15 for the esterification of acetic acid with methanol [27,28]. According to the results of the XRD analysis of the SBA-15, four main Bragg peaks were obtained (Figure 2a), corresponding to the d(100), d(110), d(200) [29,30], d(210) [31], and d(300) [32] characteristic peaks. These peaks indicate that SBA-15 has a regular mesoporous and hexagonal structure [29,30]. Moreover, losses and shifts were observed in the main Bragg peaks of the SBA-15 catalyst after loading with the active compound of Cd [27], Ti [33], or Fe [34]. The XRD peaks of the hybrid photocatalysts exhibited a broad and wide 2θ (a wide peak between 2θ = 20 and 30) [35], corresponding to the amorphous structure of SiO_2 in the SBA-15. 32.7, 44.70, 52.1, 59.2, and 64.2° values of 2θ in the SBA-15 belong to the Cd structure. They correspond to the d(101) d(102), d(110), d(112), and d(202) d-space. It shows the cubic crystal structure of CdO [30] (Figure 2b (Cd/SBA-15 10–25%)). According to the results of Fe/SBA-15 wide-angle XRD analysis, the peaks of the Fe structure were observed at 44.8 and 65.3° [33]. The diffraction peaks in the XRD spectrum were associated with the characteristic peaks of TiO_2 in the anatase phase at 2θ = 25.12 [33,36] and 47.52 [33]. They were indexed to the corresponding tetragonal crystal planes d(101) and d(200) d-space, respectively (Figure 2b) [33].

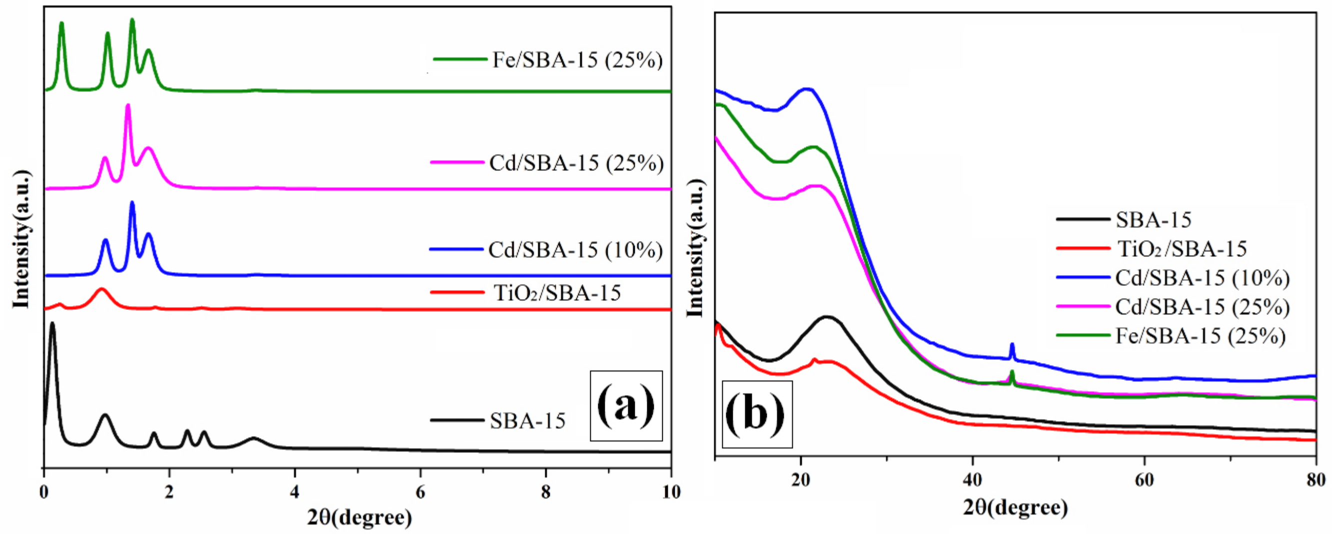

Figure 2. Low (**a**) and high (**b**)-angle XRD analyses of SBA-15, TiO_2/SBA-15 (58.33%), Fe/SBA-15 (25%), and Cd/SBA-15 (10 and 25%).

3.2. FT-IR Analysis

The FT-IR analysis of SBA-15 showed that the peaks between wavelengths of 445 cm^{-1} and 1046 cm^{-1} belonged to the characteristic structure of SBA-15 (Figure 3) [27,28]. Symmetrical and asymmetrical structures of tensile and flexible vibrations of Si-O and SiO_2 were observed at 938, 789, and 1044 cm^{-1} [37,38]. On the other hand, the peak of the wavelength 446 cm^{-1} corresponded to the Si-O-Si bending vibration [39,40]. Also, the 1377, 1444, and 650 cm^{-1} (stretching) wavelengths belonged to the Cd-S structure [37,41]. The bond signals at 580 cm^{-1} and 752 cm^{-1} were ascribed to the Ti-O stretching and Ti-O-Ti network junctions, respectively, while 959 cm^{-1} and 1080 cm^{-1}were the absorption bond signals for the Ti-OH vibrations [42]. In the SBA-15 material, the Fe (Fe-O) absorption band was observed between wavelengths of 590–615 cm^{-1} [43].

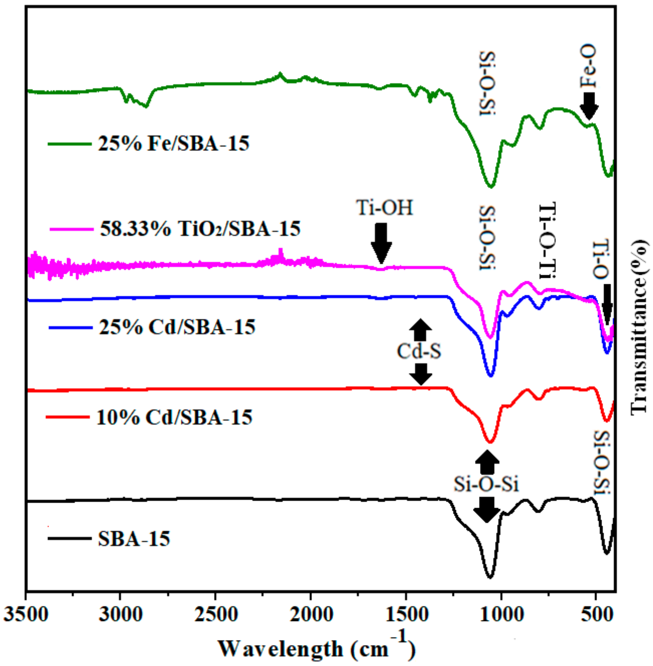

Figure 3. FT-IR analyses of calcined SBA-15, TiO_2/SBA-15 (58.33%)**,** Fe/SBA-15 (25%), and Cd/SBA-15 (10 and 25%).

3.3. SEM/EDX and Mapping Analyses

In the SEM analysis results (Figure 4a–e), wheat structures belonging to the p6 mm space groups of the calcined SBA-15 [29,44,45] were observed. On the other hand, in the SEM analyses of the uncalcined SBA-15 support material, p6mm space structures were also observed, in addition to the wheat chain structures (Figure 5a,b,d). Moreover, these structures remained after loading with Ti, Cd, and Fe (Figures 4 and 5).

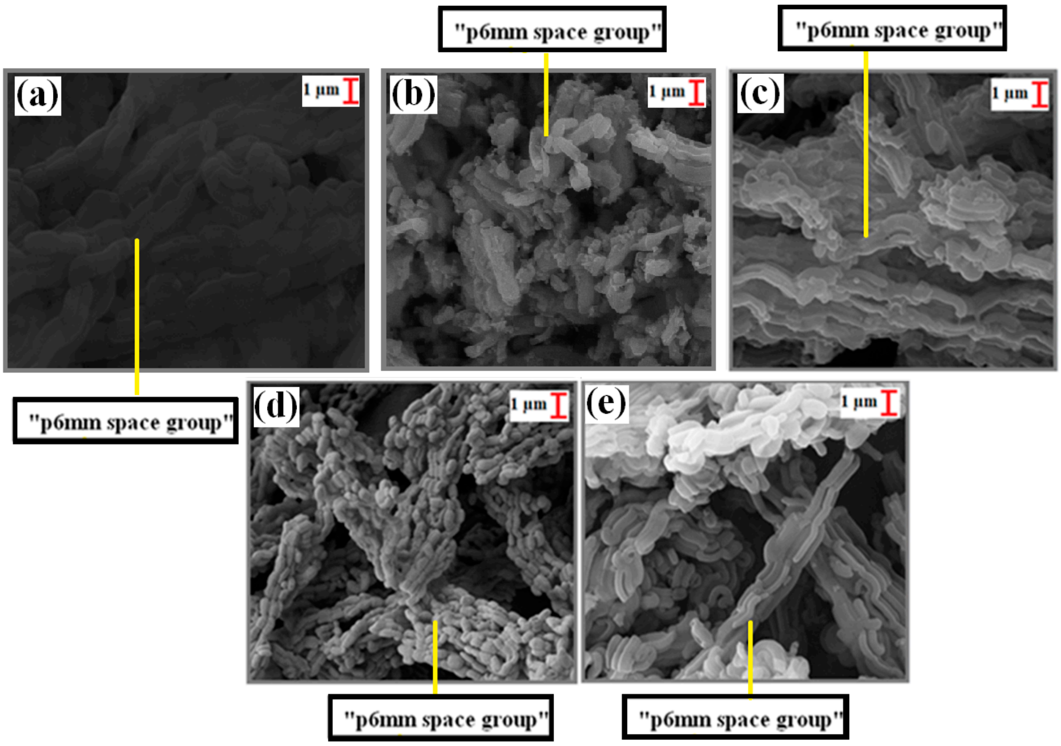

Figure 4. SEM images (10 kx) of calcinated samples: (**a**) SBA-15, (**b**) TiO_2/SBA-15 (74.30%), (**c**) Fe/SBA-15 (25%, Fe/Si), (**d**) Cd/SBA-15 (10%, Cd/Si), and (**e**) Cd/SBA-15 (25%, Cd/Si).

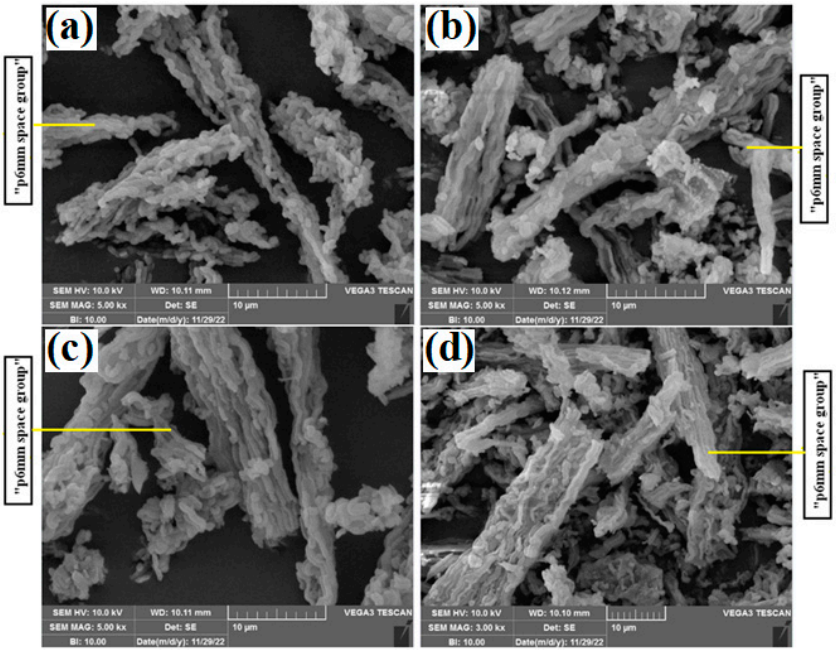

Figure 5. SEM images of uncalcinated samples: (**a**) Cd/SBA-15 (10%, Cd/Si), (**b**) Cd/SBA-15 (25%, Cd/Si), (**c**) TiO_2/SBA-15 (58.33%Ti/Si), and (**d**) SBA-15.

The results of the EDX and mapping analyses of the samples (uncalcined Cd/SBA-15 (10% and 25%) and calcined TiO_2/SBA-15 (58.33%) showed that the active compounds (Cd, Ti) were loaded on the SBA-15 support material (Figures 6 and 7). In addition, it was found that the active substances were homogeneously distributed into SBA-15 (Figure 7a–f). Figure 6 shows the Si element structure of SBA-15 without active components. The gold elements visible in the EDX results were due to the coating (they belonged to the gold particles coated before the analysis).

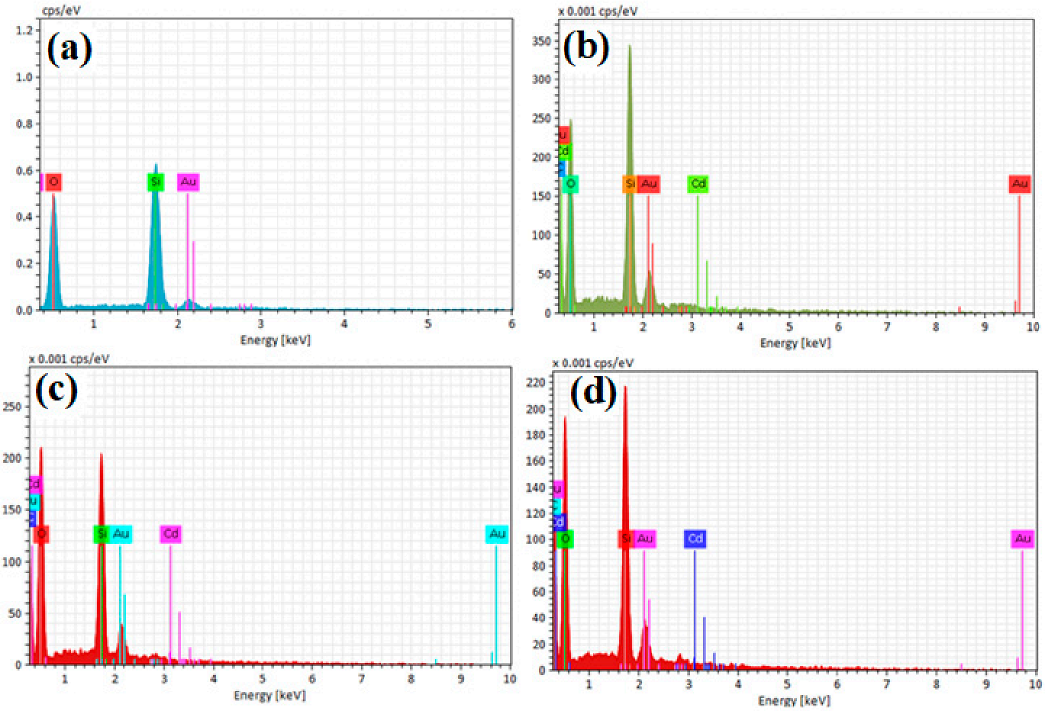

Figure 6. EDX analysis results of (**a**) uncalcined SBA-15, (**b**) uncalcined Cd/SBA-15 (10% Cd/Si), (**c**) uncalcined Cd/SBA-15 (25% Cd/Si), and (**d**) calcined TiO_2/SBA-15 (58.33% Ti/Si).

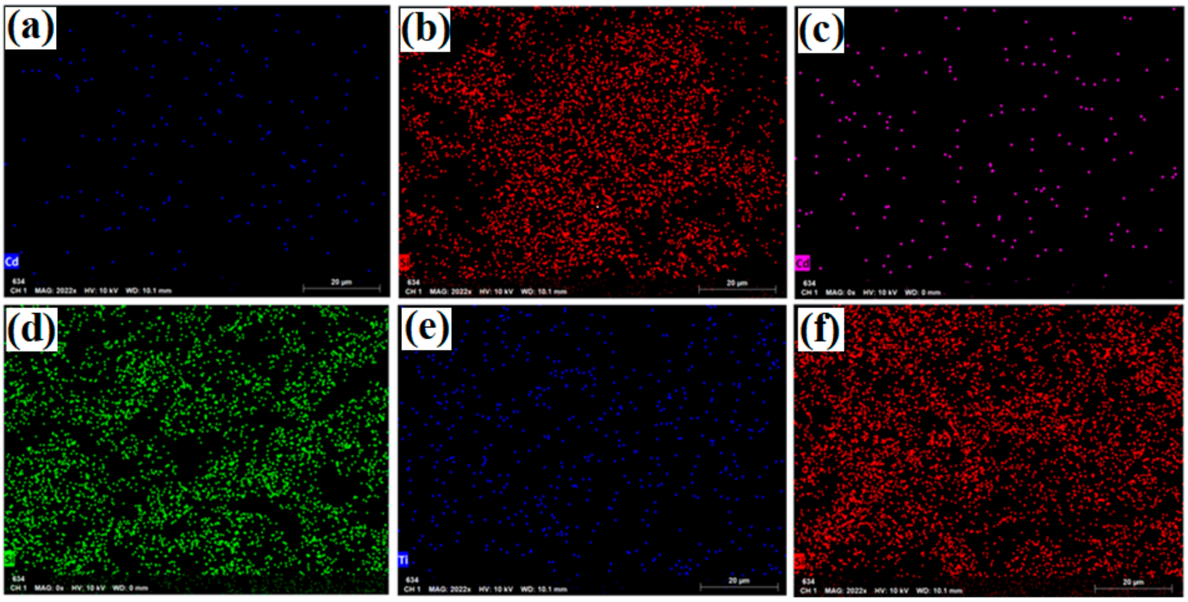

Figure 7. Mapping analysis images of: (**a**,**b**) uncalcined Cd/SBA-15 (10% Cd/Si), (**c**,**d**) uncalcined Cd/SBA-15 (25% Cd/Si),and (**e**,**f**) calcined TiO_2/SBA-15 (58.33% Ti/Si).

It is known that the calcination of solid catalysts affects the surface area, pore volume, pore diameter, and thermal stability of the support materials. As the calcination procedures were performed at suitable conditions (at 813 K for 5 h during the preparation of SBA-15 and at 623 K for 5 h during the preparation of the composite samples), no deterioration of the composite catalyst structure was observed during calcination.

3.4. Photocatalytic Activity Testing

Mesoporous silica materials, such as those of the SBA series and their related hybrid materials, have attracted considerable attention in recent decades due to their highly tunable textural and chemical properties. Therefore, they are used in various fields, including in heterogeneous catalysis for pollution remediation. This work aimed to prepare composite photocatalysts that could be used for the photocatalytic degradation of persistent neonicotinoid insecticides. For this purpose, hybrid photocatalysts consisting of the mesoporous material SBA-15 suitably modified with TiO_2, Fe, Cd, or CdS were prepared. Mesoporous SBA-15 has attracted the attention of numerous researchers since their discovery in 1998. The reason for such interest is their large specific surface area; well-defined pore structure; uniform pore size; high thermal and hydrothermal stability; and the possibility of additional functionalization with various metals, metal oxides, etc., as potential active components. There are different methods of functionalization, from direct synthesis to post-synthetic approaches, deposition—precipitation, nanoparticle encapsulation, and other methods, each with corresponding advantages and disadvantages. To overcome the shortcomings of the existing methods, different synthesis strategies are applied to determine the key parameters for choosing the best method.

Before the photocatalytic measurements, preliminary measurements were performed, which included the determination of the equilibrium adsorption of IMI on the surface of the photocatalyst without the presence of a suitable irradiation source. It was found that equilibrium adsorption occurred after about 30 min and that the IMI concentration changed slightly during this time (not shown here). Figure 8 shows the results of IMI photodegradation over TiO_2/SBA-15 nanocomposites with different TiO_2 loading (58.33–81.23%) and with unmodified SBA-15 at pH = 6.5.

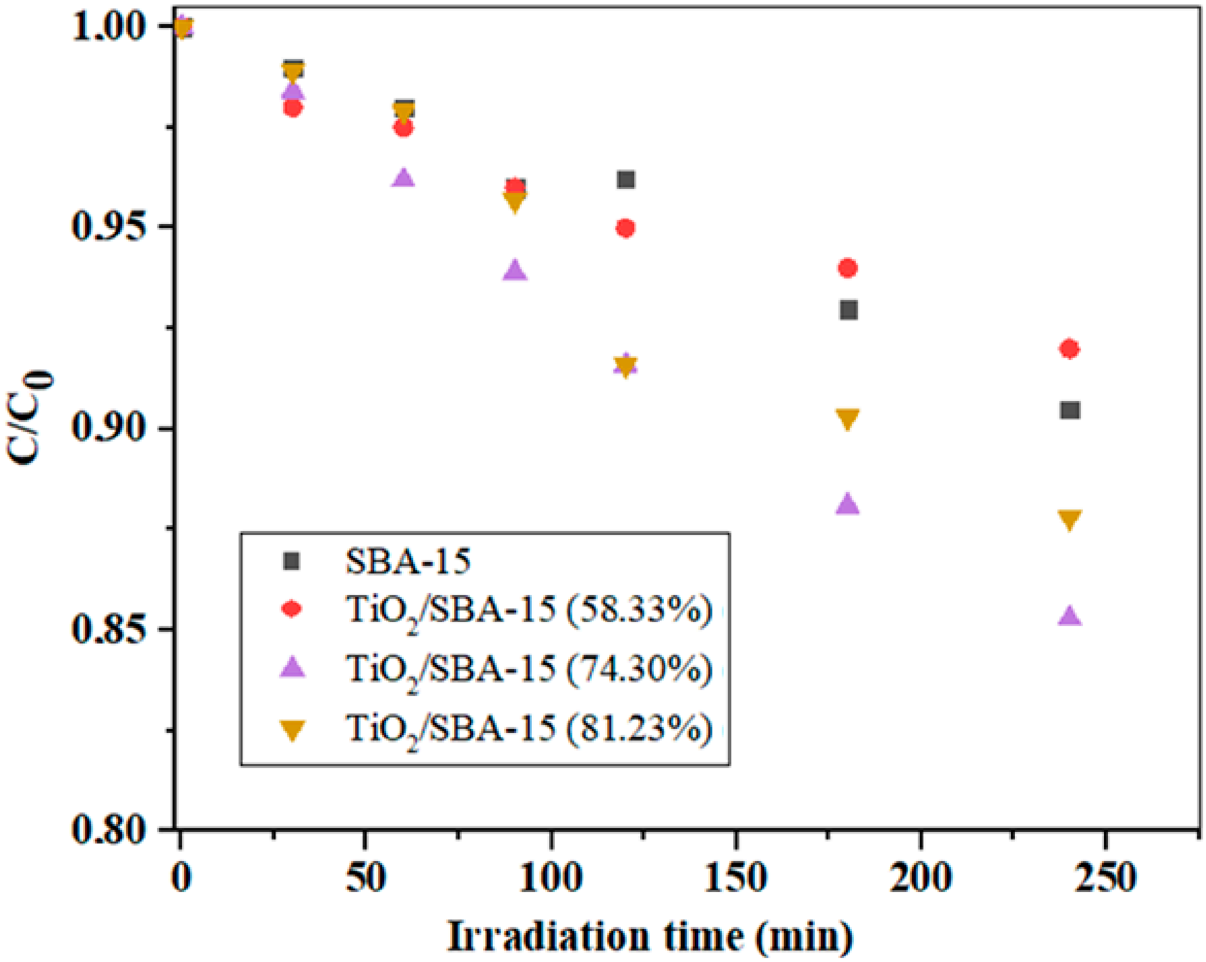

Figure 8. Photodegradation of IMI with irradiation time using uncalcinated TiO_2/SBA-15 nanocomposites with different loadings of TiO_2 (reaction performed at pH = 6.5).

As can be seen in Figure 8, the unmodified SBA-15 and the TiO_2/SBA-15 sample with 53.33 wt% TiO_2 showed similar activities at pH = 6.5. With a further increase in TiO_2 loading to 74.30%, the activity of the composite sample increased, which was confirmed by a significant decrease in the concentration of the model component, while with a further increase in TiO_2 loading to 81.23%, there was no significant increase in photoactivity. Obviously, the optimal TiO_2 loading in the TiO_2/SBA-15 sample was 74.30% under the experimental conditions specified in Figure 8. An excessive amount of TiO_2 as the active component in the composite sample could lead to a decrease in the specific surface area and in damage to the porous structure of the composite sample. In this case, the number of active sites could decrease (due to diffusion limitations) and, consequently, the photoactivity also decreased. It should be taken into consideration that the ordered mesoporous silica SBA-15 had a system of secondary mesopores (around 20 Å) and micropores, which intersected the regular structure of the parallel mesopores. Although this microporous system often facilitated the diffusion of small molecules, it also exhibited a pore-blocking effect in the sample with a higher loading of TiO_2. It is known that the pH of the reaction medium is a very important factor that affects the degradation rates of some organic compounds during the degradation process and it usually signifies the surface charge characteristics of photocatalysts [46]. The effect of pH on the removal of IMI over different photocatalysts was investigated and is illustrated in Figure 9.

The calcination procedure is another important step in the catalyst preparation that directly affects the pore volume, surface area, and pore size distribution. This is the most common method to remove organic templates that are trapped in the pores during the preparation of the mesoporous material. Although templates can be completely removed from the pores, calcination sometimes has many serious disadvantages, including possible framework shrinkage of the framework, collapse of the ordered structure, reduction in the silanol concentration at the pore wall, elimination of organic functionalities, etc. [47]. The activities in the uncalcined and calcined SBA-15-based hybrid samples examined in this study are shown and compared in Figure 9. In the case of 10% Cd/SBA-15, significantly better photodegradation of IMI was achieved with the uncalcined sample at the expected pH of 6.5. Increasing the Cd loading in the calcined sample led to a significant improvement in photoactivity compared with calcined 10% Cd/SBA-15, although the activity of this sample was still slightly lower than the activity of uncalcined 10% Cd/SBA-15. However, despite acceptable photoactivity, 25% Cd/SBA-15 showed leaching behavior when tested with the Na_2S solution, making this photocatalyst unsuitable for further testing. Further experiments were performed using Fe/SBA-15 with different iron loads (10% and 25% wt).

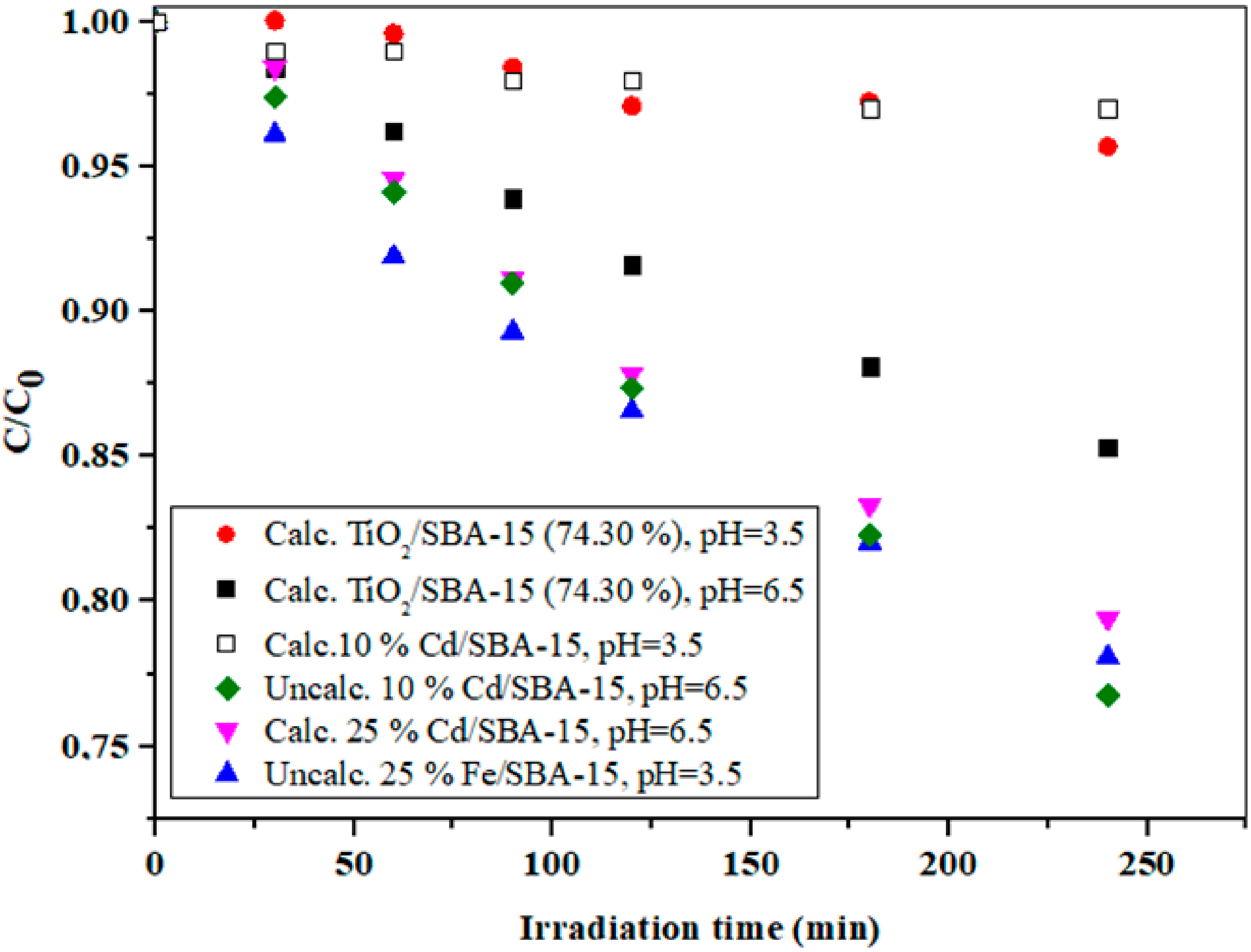

Figure 9. The effect of pH on the IMI photodegradation using TiO_2/SBA-15 (74.30%), calcinated and uncalcinated 10% Cd/SBA-15 and uncalcinated 25% Fe/SBA-15 at pH = 3.5 and/or 6.5.

Based on the results reported elsewhere [48,49], the isoelectric point (IEA) of SBA-15, which is closely related to the zero point of the surface charge, was typically between 2 and 4, which could probably be attributed to the large number of silanol groups on the surface of SBA-15. On the other hand, the IEP at a higher pH (usually around 8) was typical for iron (hydro)oxides [50]. Therefore, the rather high photocatalytic activity of 25% Fe/SBA-15 at a pH of 3.5 probably indicated that the iron was located within the pores of SBA-15 and not on the outer surface [48]. Considering that the best results for the degradation of

IMI were obtained with 10% Cd/SBA-15, further experiments were performed with this hybrid photocatalyst.

According to the literature [51,52], advanced oxidation processes based on sulfate radicals ($SO_4^{\bullet-}$) are very promising for the degradation of various organic pollutants. This can be attributed to the easy activation of peroxymonosulfate (PMS) and peroxydisulfate (PDS) to produce reactive sulfate radicals. In this context, PDS is preferred due to the higher potential, lower production costs, longer half-life, and larger O–O bond distance of PDS compared with PMS [52]. It is also known that $SO_4^{\bullet-}$ had a similar redox potential, but a longer lifetime than •OH [53,54]. The influence of the addition of PMS and PDS during the photocatalytic degradation of IMI over uncalcinated 10% Cd/SBA-15 is shown in Figure 10. As can be seen, the changes in IMI concentrations during photolytic degradation were insignificant, indicating high stability of IMI in the absence of a suitable photocatalyst. However, the efficiency of IMI degradation in the photocatalytic process was significantly improved, especially at 10% Cd-SBA-15 in the presence of PMS and PDS, resulting in almost complete IMI degradation after 240 min of irradiation. This is confirmation of the important role of PMS and PDS in the degradation of IMI. These observations can be associated with both the formation of $SO_4^{\bullet-}$ and the enhanced formation of •OH, which is due to a possible reaction of $SO_4^{\bullet-}$ with water molecules [55].

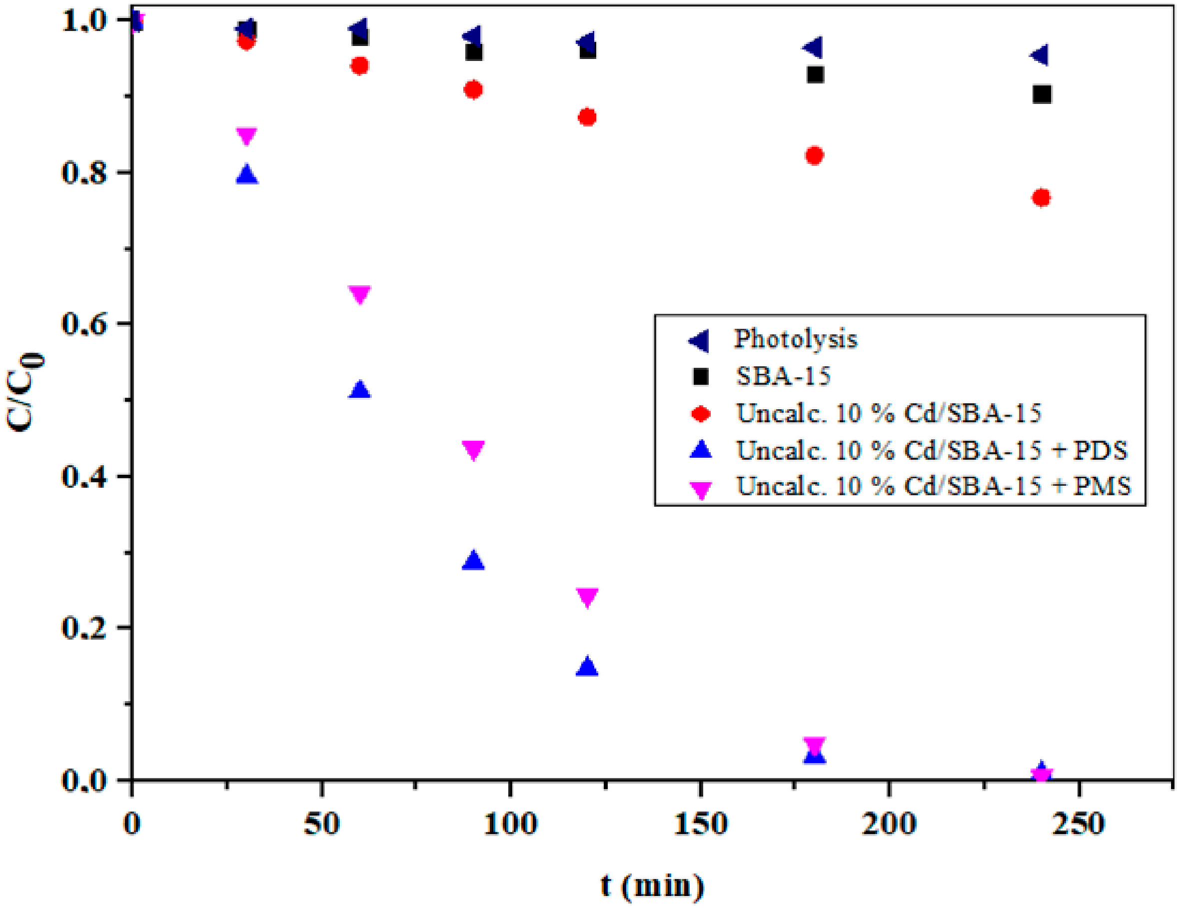

Figure 10. The influence of PMS (5 mM L^{-1}) and PDS (5 mM L^{-1}) activation over the uncalcinated 10% Cd/SBA-15 on the photocatalytic degradation of IMI (pH = 6.5).

The recoverable and reusable visible-light photocatalytic performance is of great importance for application in real systems. As shown in Figure 11, uncalcinated 10% Cd/SBA-15 showed a very stable activity in the photodegradation of the selected model component, even after several consecutive measurement cycles (240 min each + 30 min for equilibrium adsorption).

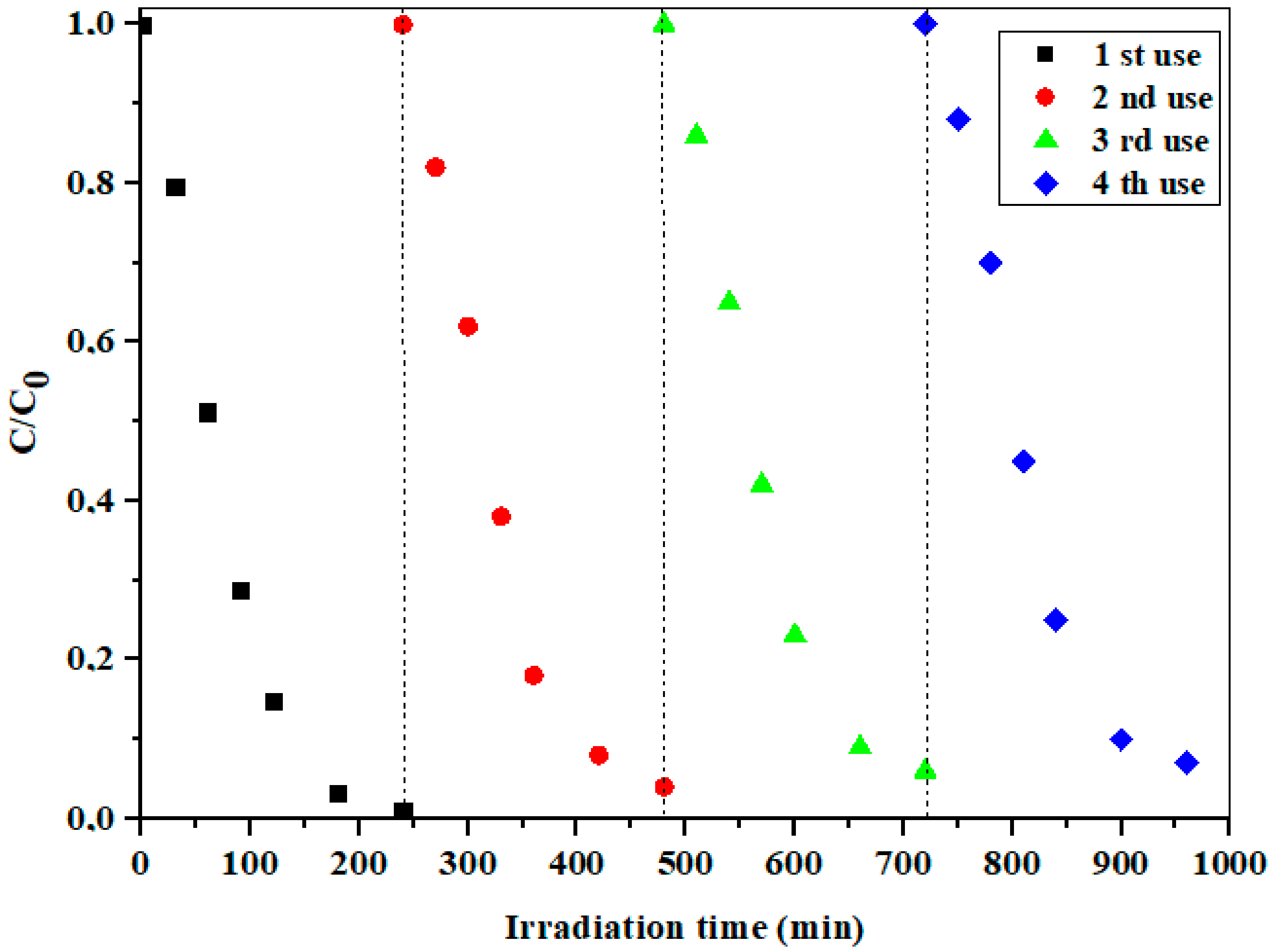

Figure 11. The reusability of the uncalcinated 10% Cd/SBA-15 in the presence of PDS at pH = 6.5.

4. Conclusions

Overall, mesoporous catalysts (especially Cd/SBA-15) show high potential for treating pesticides, such as IMI, in water. In summary, a series of SBA-based samples (SBA-15, TiO_2/SBA-15, Cd/SBA-15, and Fe/SBA-15) were prepared with different mass fractions of additional compounds for the degradation of IMI. The prepared mesoporous samples were characterized using different techniques. The IMI degradation results reported in this study show that the removal efficiency of IMI depends on the initial pH of the reaction mixture, with the best results obtained at pH = 6.5. The 10% Cd/SBA-15 possessed a higher photocatalytic activity for IMI degradation than the other mesoporous photocatalysts used in this study. The photocatalytic degradation of IMI was also carried out in the presence of PDS and PMS to improve the separation of charge carriers and increase the degradation efficiency. The efficiency of IMI degradation was significantly improved in the presence of PMS and PDS, which can be attributed to the formation of SO_4^- and the increased formation of -OH as the reactive species responsible for improved IMI degradation. Finally, Cd/SBA-15 especially in the presence of PMS and PDS as electron acceptors, shows high potential in the treatment of wastewater containing hazardous pollutants.

Author Contributions: Conceptualization, R.Z.Y. and V.T.; methodology, R.Z.Y. and V.T.; investigation, R.Z.Y., V.Ş. and L.B.; resources, R.Z.Y. and V.T.; data curation, R.Z.Y., V.Ş. and L.B.; writing—original draft preparation, R.Z.Y.; writing—review and editing, R.Z.Y., V.Ş., L.B. and V.T.; funding acquisition, R.Z.Y. and V.T. All authors have read and agreed to the published version of the manuscript.

Funding: This research was funded by Bilecik Şeyh Edebali University Scientific Research Council with project number 2022-01.BŞEÜ.03-05.

Data Availability Statement: The data presented in this study are available upon reasonable request from the corresponding authors.

Conflicts of Interest: The authors declare no conflict of interest.

References

1. Damalas, C.A.; Eleftherohorinos, I.G. Pesticide Exposure, Safety Issues, and Risk Assessment Indicators. *Int. J. Environ. Res. Public Health* **2011**, *8*, 1402–1419. [CrossRef]
2. Rajmohan, K.S.; Chandrasekaran, R.; Varjani, S. A Review on Occurrence of Pesticides in Environment and Current Technologies for Their Remediation and Management. *Indian J. Microbiol.* **2020**, *60*, 125–138. [CrossRef]
3. Shimomura, M.; Yokota, M.; Ihara, M.; Akamatsu, M.; Sattelle, D.B.; Matsuda, K. Role in the Selectivity of Neonicotinoids of Insect-Specific Basic Residues in Loop D of the Nicotinic Acetylcholine Receptor Agonist Binding Site. *Mol. Pharmacol.* **2006**, *70*, 1255–1263. [CrossRef]
4. Iwasa, T.; Motoyama, N.; Ambrose, J.T.; Roe, M.R. Mechanism for the differential toxicity of neonicotinoid insecticides in the honeybee, Apismellifera. *Crop Prot.* **2004**, *23*, 371–378. [CrossRef]
5. Jeschke, P.; Nauen, R. 5.3 Neonicotinoid Insecticides. *Elsevier Ocean. Eng. Ser.* **2006**, *5*, 53–105. [CrossRef]
6. Alex Omo Ibhadon, A.O.; Fitzpatrick, P. Heterogeneous Photocatalysis: Recent Advances and Applications. *Catalysts* **2013**, *3*, 189–218. [CrossRef]
7. Otálora, A.; Lerma, T.L.; Arrieta-Urango, Y.; Palencia, M. Emerging organic pollutants in aqueous environments: Detection, monitoring, and removal techniques. *J. Sci. Technol. Appl.* **2022**, *10*, 92–153. [CrossRef]
8. Wang, J.; Wang, S. Activation of persulfate (PS) and peroxymonosulfate (PMS) and application for the degradation of emerging contaminants. *Chem. Eng. J.* **2018**, *334*, 1502–1517.
9. Lama, G.; Meijide, J.; Sanromán, A.; Pazos, M. Heterogeneous Advanced Oxidation Processes: Current Approaches for Wastewater Treatment. *Catalysts* **2022**, *12*, 344. [CrossRef]
10. Dahl, M.; Liu, Y.; Yin, Y. Composite Titanium Dioxide Nanomaterials. *Chem. Rev.* **2014**, *114*, 9853–9889. [CrossRef] [PubMed]
11. Marques, A.C.; Vale, M.; Vicente, D.; Schreck, M.; Tervoort, E.; Niederberger, M. Porous Silica Microspheres with Immobilized Titania Nanoparticles for In-Flow Solar-Driven Purification of Wastewater. *Glob. Chall.* **2021**, *5*, 2000116. [CrossRef] [PubMed]
12. Vale, M.; Orišková, S.; Mariquito, A.; Reis, L.; Pinto, M.; Marques, A.C. Multicomponent oxide microspheres with designed macroporosity (MICROSCAFS®): A customized platform for chemicals immobilization. *RSC Adv.* **2023**, *13*, 12951–12965. [CrossRef] [PubMed]
13. Zhou, S.; Jiang, L.; Wang, H.; Yang, J.; Yuan, X.; Wang, H.; Liang, J.; Li, X.; Li, H.; Bu, Y. Oxygen Vacancies Modified TiO_2/O-Terminated Ti_3C_2 Composites: Unravelling the Dual Effects between OxygenVacancy and High-Work-Function Titanium Carbide. *Adv. Funct. Mater.* **2023**, *33*, 2307702. [CrossRef]
14. Wei, R.; Wang, H.; Jiang, L.; Yang, J.; Li, W.; Yuan, X.; Wang, H.; Liang, J.; Chen, Y.; Bu, Y. Molecular self-assembled synthesis of highly dispersed Co single-atomcoordinated 2-methylimidazole modified carbon nitride forperoxymonosulfate activation. *Chem. Eng. J.* **2023**, *471*, 144494. [CrossRef]
15. Wang, X.; Tang, W.; Jiang, L.; Yang, J.; Zhou, S.; Li, W.; Yuan, X.; Wang, H.; Wang, J.; Bu, Y. Mechanism insights into visible light-induced crystalline carbonnitride activating periodate for highly efficient ciprofloxacin removal. *Chem. Eng. J.* **2023**, *471*, 144521. [CrossRef]
16. Wu, Z.; Zhao, D. Ordered mesoporous materials as adsorbents. *Chem. Commun.* **2011**, *47*, 3332–3338. [CrossRef] [PubMed]
17. Schüth, F.; Schmidt, W. Microporous and Mesoporous Materials. *Adv. Eng. Mater.* **2002**, *4*, 269–279. [CrossRef]
18. Branković, M.D.; Zarubica, A.R.; Andjelković, T.D.; Andjelković, D.H. Mesoporoussilica (MCM-41): Synthesis/Modification, characterization and removal of selected organic micro-pollutants from water. *Adv. Technol.* **2017**, *6*, 50–57. [CrossRef]
19. Verma, P.; Kuwahara, Y.; Mori, K.; Raja, R.; Yamashita, H. Functionalized mesoporous SBA-15 silica: Recent trends and catalytic applications. *Nanoscale* **2020**, *12*, 11333. [CrossRef]
20. Sahoo, D.P.; Rath, D.; Nanda, B.; Parida, K.M. Transition metal/metal oxide modified MCM-41 for pollutant degradation and hydrogen energy production: A review. *RSC Adv.* **2015**, *5*, 83707–83724. [CrossRef]
21. Sharma, M.V.P.; Kumari, V.D.; Subrahmanyam, M. Photocatalytic degradation of Isoproturon herbicide over TiO_2/Al-MCM-41 composite system using solar light. *Chemosphere* **2008**, *72*, 644–651. [CrossRef]
22. Sharma, M.V.P.; Kumari, V.D.; Subrahmanyam, M. TiO_2 supported over SBA-15: An efficient photocatalyst for the pesticide degradation using solar light. *Chemosphere* **2008**, *73*, 1562–1569. [CrossRef]
23. Sadjadi, M.S.; Farhadyar, N.; Zare, K. Synthesis of nanosize MCM-41 loaded with TiO_2 and study of its photocatalytic activity. *Superlattices Microstruct.* **2009**, *46*, 266–271. [CrossRef]
24. Anandan, S. Photocatalytic effects of titania supported nanoporous MCM-41 on degradation of methyl orange in the presence of electron acceptors. *Dye. Pigment.* **2008**, *76*, 535. [CrossRef]
25. Ozbay, N.; Yargic, A.S.; Yarbay Sahin, R.Z.; Yaman, E. Valorization of banana peel waste via in-situ catalytic pyrolysis using Al-Modified SBA-15. *Renew. Energy* **2019**, *140*, 633–646. [CrossRef]
26. Thieleman, J.P.; Girgsdies, F.; Schlögl, R.; Hess, C. Pore structure and surface area of silica SBA-15: Influence of washing and scale-up. *Beilstein J. Nanotechnol.* **2011**, *2*, 110–118. [CrossRef]

27. Şimşek, V. Synthesis and Characterization of Fe/SBA-15 Heterogeneous Catalysts for Methyl Acetate Production. *Eur. J. Sci. Technol.* **2021**, *28*, 21–28. [CrossRef]
28. Şimşek, V. Cd/SBA-15 heterogeneous catalyst used for acetic acid conversion: Pseudo-homogeneous kinetic model, response surface methodology, and historical data design. *Z. Phys. Chem.* **2023**, *237*, 1443–1456. [CrossRef]
29. Şimşek, V. Investigation of catalytic Sustainability of Silica-Based Mesoporous Acidic Catalysts and Ion Exchange Resins in Methyl Acetate Synthesis and Characterizations of Synthesized Catalysts. *Arab. J. Sci. Eng.* **2019**, *44*, 5301–5310. [CrossRef]
30. Reza, P.H.; Sara, B. Characterization and photocatalytic activity of ZnO, ZnS, ZnO/ZnS, CdO and CdO/CdS nanoparticles in mesoporous SBA-15. *Iran. J. Chem. Chem. Eng.* **2015**, *34*, 11–19. [CrossRef]
31. Zhao, D.; Sun, J.; Li, Q.; Stucky, G.D. Morphological Control of Highly Ordered Mesoporous Silica SBA-15. *Chem. Mater.* **2000**, *12*, 275–279. [CrossRef]
32. Talha, Z.; Bachir, C.; Ziri, S.; Bellahouel, S.; Bengueddach, A.; Villièras, F.; Pelletier, M.; Weidler, P.G. Al-Rich Ordered Mesoporous Silica SBA-15 Materials: Synthesis, Surface Characterization and Acid Properties. *Catal. Lett.* **2017**, *147*, 2116–2126. [CrossRef]
33. Toro, R.G.; Diab, M.; de Caro, T.; Al-Shemy, M.; Adel, A.; Caschera, D. Study of the Effect of Titanium Dioxide Hydrosol on the Photocatalytic and Mechanical Properties of Paper Sheets. *Materials* **2020**, *13*, 1326. [CrossRef] [PubMed]
34. Huang, H.; Ji, Y.; Qiao, Z.; Zhao, C.; He, J.; Zhang, H. Preparation, Characterization, and Application of Magnetic Fe-SBA-15 Mesoporous Silica Molecular Sieves. *Hindawi Publ. Corp. J. Autom. Methods Manag. Chem.* **2010**, *7*, 323509. [CrossRef] [PubMed]
35. Mikheeva, N.N.; Zaikovskii, V.I.; Mamontov, G.V. Synthesis of ceria nanoparticles in pores of SBA-15: Pore size effect and influence of citric acid addition. *Microporous Mesoporous Mater.* **2019**, *277*, 10–16. [CrossRef]
36. Shen, H.; Tang, Z.; Xiao, X.; Wu, H.; Zhou, H.; Fang, P.; Zhu, D.; Ge, J. Catalytic Oxidation of NO by Ozone over Mn-Ce/Al_2O_3/TiO_2 Catalyst. *Processes* **2022**, *10*, 1946. [CrossRef]
37. Junhong, W.J.; Shao, X.; Liu, J.; Ji, X.; Ma, J.; Tian, G. Fabrication of CdS-SBA-15 nanomaterials and their photocatalytic activity for degradation of salicylic acid under visible light. *Ecotoxixology Environ. Saf.* **2020**, *190*, 110139.
38. Ziarani, G.M.; Ebrahimi, Z.; Mohajer, F.; Alireza, B. Fluorescent Chemosensor Based on Functionalized Nanoporous Silica (SBA-15 SBA-IC-MN) for Detection of Hg^{2+} in Aqueous Media. *Arab. J. Sci. Eng.* **2021**, *47*, 397–406. [CrossRef]
39. Bhuyan, D.; Selvaraj, K.; Saikia, L. Pd/SBA-15 nanocomposite catalyst: Synthesis and efficient solvent-free semihydrogenation of phenylacetylene under mild conditions. *Microporous Mesoporous Mater.* **2017**, *241*, 266–273. [CrossRef]
40. Yarbay Şahin, R.Z. A comparative study on dark adsorption of dyes using mesoporous MCM-41 catalyst. *Res. Chem. Intermed.* **2022**, *48*, 541–553. [CrossRef]
41. Kumar, S.; Sharma, J.K. Stable phase CdS nanoparticles for optoelectronics: A study on surface morphology, structural and optical characterization. *Mater. Sci.-Pol.* **2016**, *34*, 368–373. [CrossRef]
42. Anucha, C.B.; Bacaksiz, E.; Stathopoulos, V.N.; Pandis, P.K.; Argirusis, C.; Andreouli, C.-D.; Tatoudi, Z.; Altin, I. Molybdenum Modified Sol–Gel Synthesized TiO2 for the Photocatalytic Degradation of Carbamazepine under UV Irradiation. *Processes* **2022**, *10*, 1113. [CrossRef]
43. Bin, M.; Tingmei, W.; Zhenhua, W.; Huigang, S.; Desheng, X.; Peng, L. Fabrication of functional block copolymer grafted superparamagnetic nanoparticles for targeted and controlled drug delivery. *Colloids Surf. A Physicochem. Eng. Asp.* **2011**, *375*, 163–168. [CrossRef]
44. Sayari, A.; Han, B.H.; Yang, Y. Simple synthesis route to monodispersed SBA-15 silica rods. *J. Am. Chem. Soc.* **2004**, *126*, 14348–14349. [CrossRef]
45. Simsek, V. Synthesis, Characterization and Investigation Catalytic Activity in the Glycerol Esterification Reaction of Acidic Catalyst. Ph.D. Thesis, Gazi University Graduate School of Natural and Applied Sciences, Ankara, Türkiye, 2015.
46. Sudhaik, A.; Raizada, P.; Thakur, S.; Saini, R.V.; Saini, A.K.; Singh, P.; Thakur, V.K.; Nguyen, V.H.; Khan, A.A.P.; Asiri, A.M. Synergistic photocatalytic mitigation of imidacloprid pesticide and antibacterial activity using carbon nanotube decorated phosphorus doped graphitic carbon nitride photocatalyst. *J. Taiwan Inst. Chem. Eng.* **2020**, *113*, 142–154. [CrossRef]
47. Ghaedi, H.; Zhao, M. Review on Template Removal Techniques for Synthesis of Mesoporous Silica Materials. *Energy Fuels* **2022**, *36*, 2424–2446. [CrossRef]
48. Ruchomski, L.; Pikus, S.; Pikula, T.; Mączka, E.; Marek Kosmulski, M. Synthesis and properties of Fe/SBA-15. *Colloids Surf. A Physicochem. Eng. Asp.* **2020**, *599*, 124922. [CrossRef]
49. Colilla, M.; Martínez-Carmona, M.; Sánchez Salcedo, S.; Ruiz-González, M.L.; González-Calbetc, J.M.; Vallet-Regí, M. A Novel Zwitterionic Bioceramicwith Dual Antibacterial Capability. *J. Mater. Chem. B* **2014**, *2*, 5639–5651. [CrossRef]
50. Kosmulski, M. Isoelectricpoints and points of zero charge of metal (hydr)oxides: 50 years after Parks' review. *Adv. Colloid Interf. Sci.* **2016**, *238*, 1–61. [CrossRef]
51. Urán-Duque, L.; Saldarriaga-Molina, J.C.; Rubio-Clemente, A. Advanced Oxidation Processes Based on Sulfate Radicals for Wastewater Treatment: Research Trends. *Water* **2021**, *13*, 2445. [CrossRef]
52. Hasija, V.; Nguyen, V.H.; Kumar, A.; Raizada, P.; Krishnan, V.; Khan, A.A.P.; Singh, P.; Lichtfouse, E.; Wang, C.; Thi Huong, P. Advanced Activation of Persulfate by Polymeric G-C_3N_4 Based Photocatalysts for Environmental Remediation: A Review. *J. Hazard. Mater.* **2021**, *413*, 125324. [CrossRef] [PubMed]
53. Li, H.; Shang, J.; Yang, Z.; Shen, W.; Ai, Z.; Zhang, L. Oxygen Vacancy Associated Surface Fenton Chemistry: Surface Structure Dependent Hydroxyl Radicals Generation and Substrate Dependent Reactivity. *Environ. Sci. Technol.* **2017**, *51*, 5685–5694. [CrossRef] [PubMed]

54. Oh, W.D.; Dong, Z.; Lim, T.T. Generation of Sulfate Radical through Heterogeneous Catalysis for Organic Contaminants Removal: Current Development, Challenges and Prospects. *Appl. Catal. B* **2016**, *194*, 169–201. [CrossRef]
55. Wang, Q.; Rao, P.; Li, G.; Dong, L.; Zhang, X.; Shao, Y.; Gao, N.; Chu, W.; Xu, B.; An, N. Degradation of imidacloprid by UV-activated persulfate and peroxymonosulfate processes: Kinetics, impact of key factors and degradation pathway. *Ecotoxicol. Environ. Saf.* **2020**, *187*, 109779. [CrossRef]